Simulating the formation of a sigmoidal flux rope in AR10977 from SOHO/MDI magnetograms

Gibb, G. P. S.; MacKay, D. H.; Green, L. M.; Meyer, K. A.

Published in:
Astrophysical Journal

DOI:
10.1088/0004-637X/782/2/71

Publication date:
2014

Document Version
Publisher's PDF, also known as Version of record

The Astrophysical Journal, 782:71 (14pp), 2014 February 20 doi:10.1088/0004-637X/782/2/71

SIMULATING THE FORMATION OF A SIGMOIDAL FLUX ROPE IN AR10977 FROM *SOHO*/MDI MAGNETOGRAMS

G. P. S. Gibb[1], D. H. Mackay[1], L. M. Green[2], and K. A. Meyer[1]
[1] University of St Andrews, School of Mathematics and Statistics, North Haugh, St Andrews, Fife KY16 9SS, UK
[2] University College London, Mullard Space Science Laboratory, Holmbury St. Mary, Dorking, Surrey RH5 6NT, UK
Received 2013 September 27; accepted 2013 December 18; published 2014 January 29

ABSTRACT

The modeling technique of Mackay et al. is applied to simulate the coronal magnetic field of NOAA active region AR10977 over a seven day period (2007 December 2–10). The simulation is driven with a sequence of line-of-sight component magnetograms from *SOHO*/MDI and evolves the coronal magnetic field though a continuous series of non-linear force-free states. Upon comparison with *Hinode*/XRT observations, results show that the simulation reproduces many features of the active region's evolution. In particular, it describes the formation of a flux rope across the polarity inversion line during flux cancellation. The flux rope forms at the same location as an observed X-ray sigmoid. After five days of evolution, the free magnetic energy contained within the flux rope was found to be 3.9×10^{30} erg. This value is more than sufficient to account for the B1.4 *GOES* flare observed from the active region on 2007 December 7. At the time of the observed eruption, the flux rope was found to contain 20% of the active region flux. We conclude that the modeling technique proposed in Mackay et al.—which directly uses observed magnetograms to energize the coronal field—is a viable method to simulate the evolution of the coronal magnetic field.

Key words: Sun: corona – Sun: coronal mass ejections (CMEs) – Sun: flares – Sun: X-rays, gamma rays

Online-only material: animations, color figures

1. INTRODUCTION

Soft X-ray images of the Sun have shown S- or inverted S-shaped emission features within active regions (ARs). These features are called sigmoids (Rust & Kumar 1996) and were first observed by *Skylab*, and later by *Yohkoh*/SXT. ARs with sigmoids are statistically more likely to host eruptions than ARs without sigmoids (Canfield et al. 1999; Glover et al. 2000). Rust & Kumar (1996) noted that sigmoids in the southern hemisphere tended to be S-shaped, while those in the northern hemisphere tended to be inverse S-shaped. This suggests that sigmoids have negative magnetic helicity in the northern hemisphere and positive magnetic helicity in the southern hemisphere, in agreement with the findings of Pevtsov et al. (1995).

Rust & Kumar (1996) proposed that sigmoids are the projections of helically kinked flux ropes (FRs) along the line of sight (LOS). To appear as an S-shape in projection, they argue that the FR would require a twist around its axis of $\approx 2\pi$. They calculated that the majority of FRs with such a twist would be kink unstable and thus would eventually erupt. Titov & Démoulin (1999), however, suggested that sigmoids are emission from a current layer in a separatrix surface formed by bald patch field lines underneath an FR. The works of Canfield et al. (2007) and Green et al. (2007) favor the Titov & Démoulin (1999) sigmoid model over the Rust & Kumar (1996) model.

The origin of FRs in the corona are now discussed. van Ballegooijen & Martens (1989) proposed a mechanism whereby an FR may form in situ in the corona. In this scenario, a sheared arcade is gradually transformed into an FR by shearing and converging photospheric motions driving reconnection at a polarity inversion line (PIL). Multiple reconnection events then produce the FR. In contrast, Rust & Kumar (1994) suggested that an FR produced in the convective zone may rise due to magnetic buoyancy and emerge through the photosphere into the corona. Numerous numerical studies have shown, however, that the axis of the FR is unable to rise through the photosphere and results in a sheared arcade in the corona (Fan 2001; Moreno-Insertis 2004; Archontis et al. 2004; Archontis 2008). Even though this is the case, an FR may still form from these sheared arcade field lines, either through rotation of the emerged flux, twisting the arcade into an FR (Magara 2006; Fan 2009; Leake et al. 2013), or through reconnection transforming the arcade into an FR in a manner consistent with the van Ballegooijen & Martens (1989) mechanism (Manchester et al. 2004; Archontis & Török 2008; Archontis & Hood 2010).

There are several mechanisms by which an FR can become unstable and erupt. The FR may undergo a loss of equilibrium through an ideal magnetohydrodynamical (MHD) instability (Hood & Priest 1981; Kliem & Török 2006). The FR could also experience a force imbalance between itself and the arcade above it, whereby the upward Lorentz force from the FR dominates over the downward tension force of the arcade (Mackay & van Ballegooijen 2006). Several studies (Bobra et al. 2008; Su et al. 2009; Savcheva & van Ballegooijen 2009) have shown that the force imbalance occurs when the ratio of FR flux to AR flux exceeds 10%–14%.

As the magnetic field within the corona cannot presently be measured, it must be inferred from simulations or from extrapolations of the measured photospheric magnetic field. The corona may be approximated as being "force-free," given by the expression $\mathbf{j} \times \mathbf{B} = 0$, where $\mathbf{j}$ and $\mathbf{B}$ are the current density and magnetic flux density, respectively. Hence, $\mathbf{j} = \alpha \mathbf{B}$, where $\alpha = \alpha(\mathbf{r})$ is a scalar function of position, but is constant along a magnetic field line. The simplest force-free field is defined as a field with zero current everywhere ($\alpha = 0$), called a potential field. This field is not useful for determining the energy available for eruptions, as a potential field is the lowest energy field given a prescribed boundary condition. The next step up in complexity is a linear force-free (LFF) field where α is constant everywhere. This is unphysical, however, since if the whole corona was

described by an LFF field, then the energy content would be infinite (Seehafer 1978). The case where α is a function of position $\alpha = \alpha(\mathbf{r})$, a nonlinear force-free (NLFF) field, is the most realistic.

Much work has been carried out in developing methods of generating NLFF fields from magnetogram data. This can be achieved by either extrapolating the NLFF field from a single vector magnetogram directly, or by evolving an initial field—typically a potential or LFF—into an NLFF state. Examples of extrapolations are Low & Lou (1990), Wheatland et al. (2000), Liu et al. (2002), Yan & Sakurai (1997, 2000), and Régnier et al. (2002). The magnetofrictional method (Yang et al. 1986) has been used by a number of authors to produce single snapshots of NLFF fields. One method is to take a potential field extrapolated from a magnetogram and set the photospheric field to be that of the vector magnetogram. The coronal field is then allowed to relax to an NLFF state (Valori et al. 2005). An alternative method involves inserting an FR into a potential field, and relaxing the field into an NLFF state (van Ballegooijen 2004; Savcheva et al. 2012). A key feature of the above methods is that they take a single magnetogram frame, and from it derive a single NLFF field. Using these methods and taking a time series of magnetograms, a time series of independent NLFF fields may be extrapolated. It is important to note, however, that each NLFF field produced is independent of the previous fields in the time series, and hence this technique does not reflect a true time-evolution of the coronal field, as no information is transferred between subsequent times. In contrast to the single extrapolation method, the magnetofrictional method may be used to generate a continuous time series of NLFF fields by evolving an initial coronal field through changing the photospheric magnetic field continuously according to a time series of synthetic or observed magnetograms (van Ballegooijen et al. 2000; Mackay & van Ballegooijen 2006; Yeates et al. 2007; Mackay et al. 2011; Cheung & DeRosa 2012; Meyer et al. 2013b). Using this method, the time series of NLFF fields is now dependent upon previous magnetic configurations and field line connectivity.

Mackay et al. (2011) apply the magnetofrictional method along with LOS magnetograms to simulate the evolution of a dispersing AR's coronal magnetic field. By doing so they quantify the energy and helicity input into the corona. They did not, however, carry out any comparison of the simulation with coronal images. Additionally, the four day period simulated by Mackay et al. (2011) did not include any significant flux cancellation. In the present study, we extend this work to simulate the evolution of the coronal field of AR10977—in particular its emergence phase, followed by a decay phase with significant flux cancellation and formation of an observed X-ray sigmoid. As such, this paper may be considered a follow-on study to Mackay et al. (2011). A key new feature of the present study over that of Mackay et al. (2011) is that we apply a simple method to produce emission proxy images such that we may directly compare the simulation results with coronal observations of the AR. By doing so we may determine whether or not the photospheric boundary technique of Mackay et al. (2011) can reproduce the evolution seen in the coronal images. We also examine in detail the formation and properties of the FR produced in our simulation.

In order to verify the validity of the modeling method of Mackay et al. (2011), we study the previously considered AR10977 so that we may carry out a qualitative and quantitative comparison of our results with previous studies of this AR. Only by doing this can we determine if the modeling technique of Mackay et al. (2011), which solely uses normal component magnetograms, is a viable method of simulating the coronal field. While AR10977 has been studied before, we note that this is the first study that considers a continuous time evolution of its coronal magnetic field though simulation. We note here that Cheung & DeRosa (2012) carried out a similar simulation of a different AR. They found that the use of normal component magnetograms alone was insufficient to reproduce the coronal images. In order to produce a good agreement, an extra twisting motion on the boundary had to be applied.

AR10977 has previously been studied by Green et al. (2011) and Savcheva et al. (2012). Green et al. (2011) used observations to determine that the sigmoid was associated with an FR, and that the formation mechanism of the FR was consistent with that of the mechanism proposed by van Ballegooijen & Martens (1989). Additionally, they found that the flux contained within the FR was at most 60% of the AR flux, though more likely to be around 30%. Savcheva et al. (2012) carried out NLFF field extrapolations of AR10977's coronal field using the FR insertion method of van Ballegooijen (2004). This process was carried out at various times to obtain an estimate for the variation of the AR's properties. The results from this study showed that the best-fit FR contained roughly 50% of the AR flux, the free magnetic energy was roughly 6×10^{30} erg, and the helicity was 3×10^{41} Mx^2.

The paper is structured as follows. Section 2 outlines the observations of AR10977, Section 3 describes various properties of the AR, Section 4 describes the simulation method, Section 5 describes the results of the simulation, and Section 6 discusses the results and draws conclusions.

2. OBSERVATIONS

AR10977 was observed on the Sun's southern hemisphere between the 2nd and 10th of 2007 December. During this period, the AR's full lifetime—from emergence to decay—was observed.

The evolution of the AR's photospheric magnetic field as observed by *SOHO*/MDI over this period of time can be seen in Figure 1. At the start of the observations (2007 December 2), the AR has a simple bipolar configuration, aligned east–west (top left, Figure 1). For the first two days of the observations the AR was still in the emergence phase. During this time, it rotated clockwise (CW; top center, Figure 1). Starting on 2007 December 4 and continuing on 2007 December 5, flux cancellation occurred across the PIL between the two polarities. With this the negative polarity region fragmented (top right, Figure 1) where the fragmentation of the negative polarity continued over the next few days. On 2007 December 5, the AR began to rotate counter-clockwise (CCW; bottom left, Figure 1). A second flux cancellation event occurred late on December 7, continuing into December 8 (bottom center, Figure 1). Finally, the AR began to diffuse away, and continued to rotate CCW (bottom right, Figure 1).

The evolution of the coronal magnetic field above the AR can be seen through X-ray images taken by the X-Ray Telescope (XRT) on the Japan Aerospace Exploration Agency (JAXA)'s *Hinode* space telescope. Figure 2 shows a collection of four images from XRT illustrating the later stages of the evolution of the AR's coronal field. The images show a magnetic field structure that initially looks like an arcade (Figure 2, top left), then becomes more sheared due to the bipole's rotation (Figure 2, top right). On 2007 December 6, the X-ray

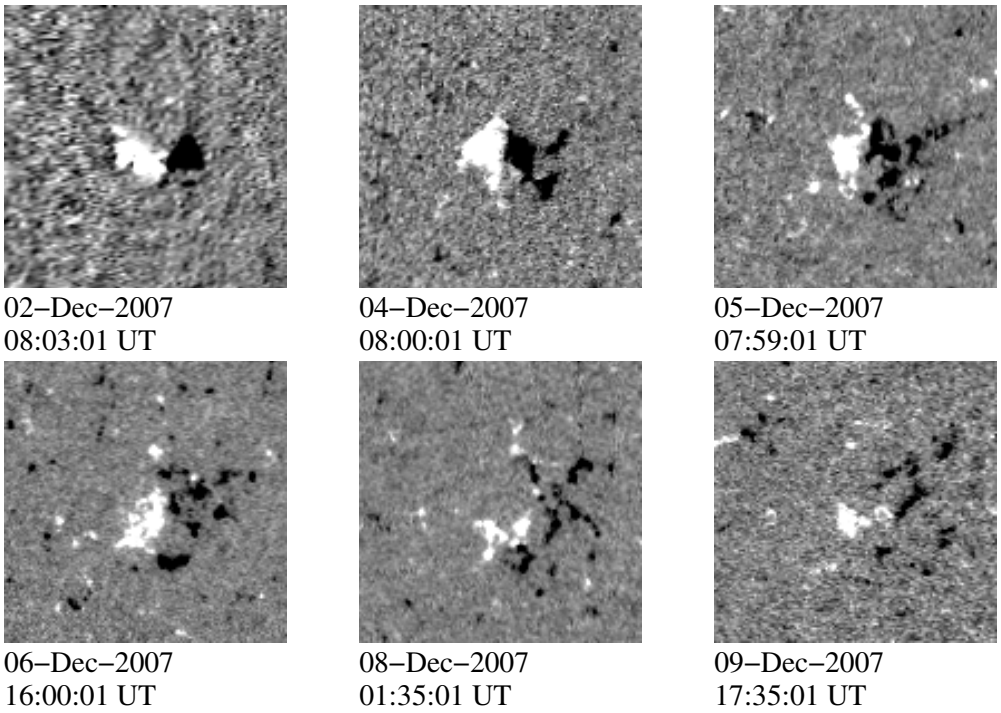

Figure 1. Time sequence of derotated *SOHO*/MDI line-of-sight magnetograms of AR10977 from 2007 December 2–9. The white areas represent positive magnetic polarities and black areas represent negative magnetic polarities. The images saturate at ±100 G.

emission takes on the appearance of a continuous forward S-shape—a sigmoid (Figure 2, bottom left). This sigmoid grows in size (Figure 2, bottom right) and then a B1.4-class *GOES* flare occurs at around 04:20 UT on 2007 December 7. The flare was associated with an eruption and the temporary disappearance of the sigmoid. Green et al. (2011) proposed that the sigmoid contained an FR that became unstable and then either fully or partly erupted.

3. ACTIVE REGION PROPERTIES

To simulate the evolution of the coronal magnetic field of AR10977, the magnetograms discussed in Section 2 are used as lower boundary conditions in the simulation. Due to their noisy nature, they must be cleaned up before they can be used. The clean-up process is described in Appendix A, where a number of steps are applied (e.g., noise reduction, removal of isolated fields below |25| G, and flux balancing). These steps are designed to remove small scale random magnetic elements but retain the overall evolution of the large-scale polarities within the AR. In this section, we provide the properties of AR10977 deduced from the cleaned magnetograms.

Figure 3(a) shows the variation of both the positive (dashed line) and unsigned negative flux (dotted line) prior to flux balance, and the flux-balanced total flux divided by two (solid line) within the AR. From this figure it is clear that both the positive and negative polarities follow a similar behavior before and after the flux balancing has been applied. The plot starts at 08:03 UT on 2007 December 2, corresponding to the sixth frame from the original set of observations. From Figure 3(a) it can be seen that both the positive and negative AR flux increases over the first two days of observations due to flux emergence. After the second day, it decreases mainly due to two significant flux cancellation events on 2007 December 5 and 7 (denoted by the vertical dashed lines in Figures 3(a), 4 and 11). Within each of these events approximately 3×10^{20} Mx is canceled. These correspond to the cancellation events seen in Figure 1 (top center and bottom center). Figure 3(b) shows the flux imbalance before (solid line) and after (dash-dotted line) the correction.

In Figure 4, the variation of the tilt angle as a function of time is plotted. The solid line is the tilt angle after flux balance while the stars denote the tilt angle prior to flux balancing. Both tilt angles show a similar evolution where it can be seen that the flux correction—which is necessary to run the three-dimensional (3D) simulation—does not change the overall behavior of the AR. The tilt angle is defined as the angle that the vector directed from the center of flux (COF) of the positive polarity region to the COF of the negative region makes with the east–west line. The calculation of the tilt angle is described in Appendix B. From the start of the observations until 2007 December 4, the negative polarity region rotates CW, with the tilt angle becoming negative, peaking around -10°. However, late on 2007 December 5, the rotation of the negative polarity reverses to CCW, where the tilt angle increases toward positive values almost linearly for the remaining duration of the observations.

4. THE SIMULATION

A magnetofrictional relaxation method is used to simulate the coronal magnetic field of AR10977. By using this, a continuous time series of NLFF fields is generated from the time series of magnetograms. These fields preserve magnetic connectivity and flux from one time to the next and thus allow the evolution of the coronal field to be studied. This is in stark contrast to independent coronal field extrapolations, which do not preserve these quantities. The magnetofrictional method was first proposed by Yang et al. (1986), and has been applied in previous studies to consider the hemispheric pattern of solar filaments (Mackay & van Ballegooijen 2005), the formation of filament channels (van Ballegooijen et al. 2000; Mackay & Gaizauskas 2003), and the formation of FRs (Mackay &

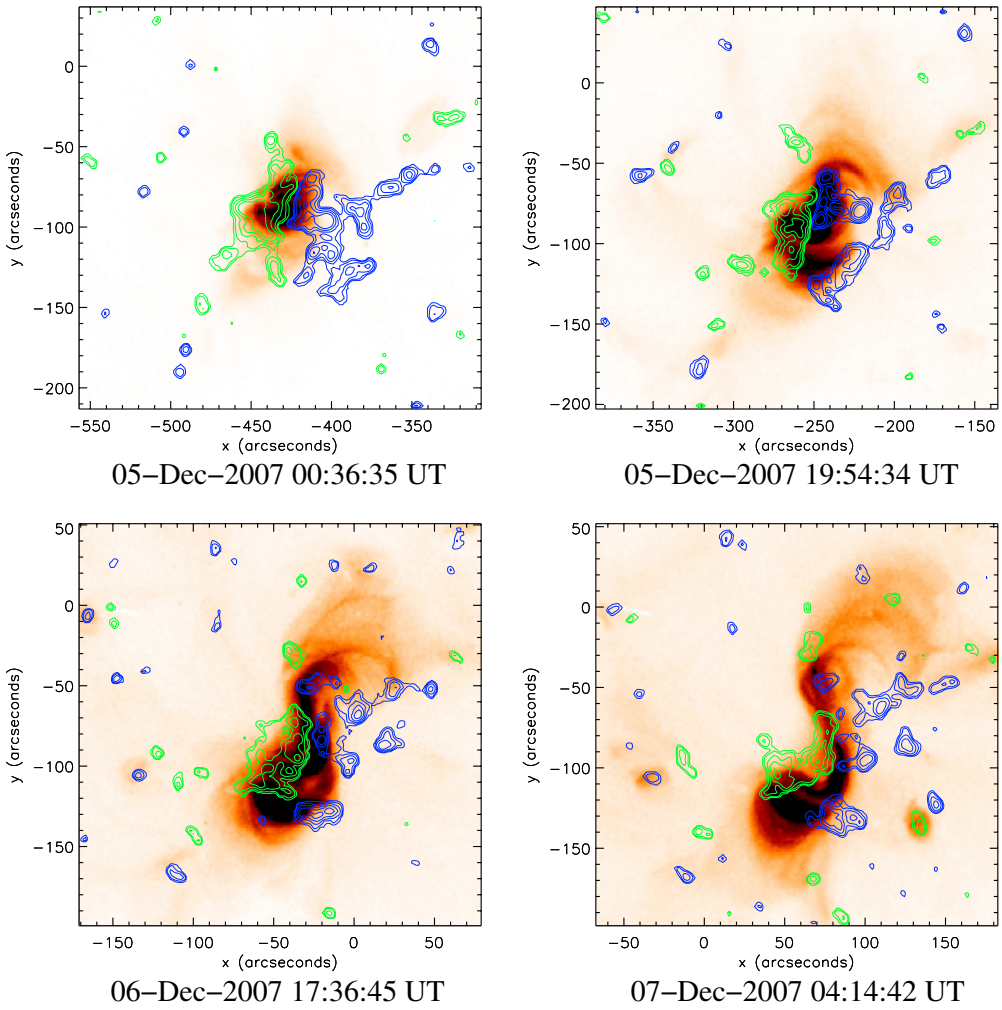

Figure 2. Selection of XRT images outlining the evolution of the emission from an unsheared arcade field (top left), to a sheared field (top right), a sigmoid (bottom left) which increases in size (bottom right). The green contours denote positive magnetic flux on the photosphere, and the blue contours denote negative magnetic flux. (A color version of this figure is available in the online journal.)

van Ballegooijen 2006). In the present study, we apply the same coronal modeling and photospheric evolution method as that described in Mackay et al. (2011). A description of this technique is given below. We note that this modeling method is similar to that employed in Cheung & DeRosa (2012).

The 3D magnetic field **B** is evolved according to the ideal induction equation,

$$\frac{\partial \mathbf{A}}{\partial t} = \mathbf{v} \times \mathbf{B}, \tag{1}$$

where **A** is the magnetic vector potential such that $\mathbf{B} = \nabla \times \mathbf{A}$ and **v** is the magnetofrictional velocity.

In the magnetofrictional approach, the equation of motion is modified to include an artificial frictional term of the form $\nu'\mathbf{v}$, where ν' is a frictional coefficient. Under the steady state approximation and neglecting any external forces, the equation of motion reduces to

$$\mathbf{j} \times \mathbf{B} - \nu'\mathbf{v} = 0, \tag{2}$$

where $\mathbf{j} = \nabla \times \mathbf{B}$. The magnetofrictional velocity **v** can thus be prescribed as

$$\mathbf{v} = \frac{\mathbf{j} \times \mathbf{B}}{\nu'}. \tag{3}$$

The form of the frictional coefficient is taken to be

$$\nu' = \nu B^2, \tag{4}$$

where ν is a constant, which results in the frictional relaxation velocity being independent of the magnetic field strength. The relaxation velocity is thus aligned in the direction of the Lorentz force and acts to restore any perturbed field toward an equilibrium configuration. In the simulation, ν is taken to be 2.28×10^{-10} m^{-2} s. This value is chosen such that the angle between **j** and **B** during the quasi-static evolution remains less than 1°. This ensures that the magnetic field at all times in the simulation remains very close to an NLFF state.

The simulation uses a Cartesian frame of reference. A staggered grid is used for the variables **A**, **B**, and **j** to ensure second-order accuracy. The primary variable is the magnetic vector potential, **A**, since its use automatically ensures that $\nabla \cdot \mathbf{B} = 0$ is satisfied. The computational box represents an isolated region of the Sun, with the photosphere located at the bottom of the box. Closed boundary conditions (BCs) are used on the top and sides of the box, while the lower BC is prescribed by the observed magnetograms. The BCs require flux to only enter and leave the computational box via the base of the box. Thus, to ensure the solenoidal constraint is satisfied,

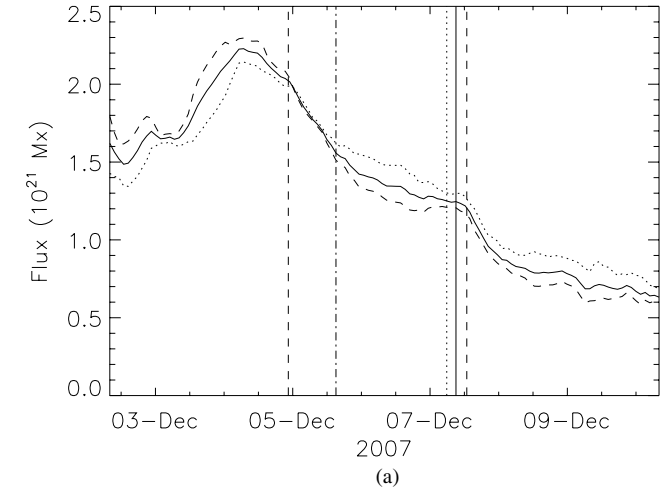

(a)

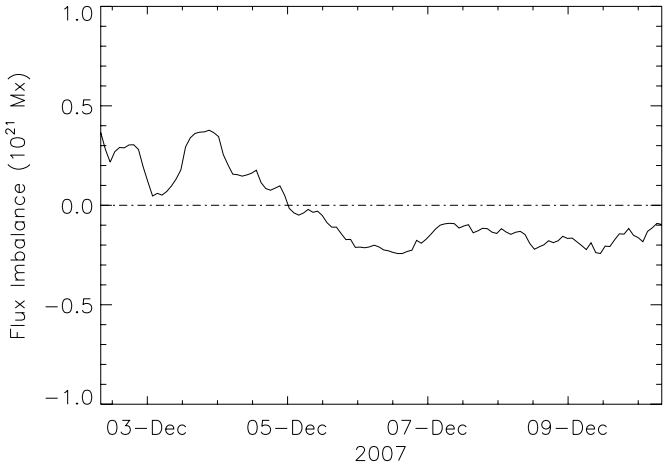

(b)

Figure 3. (a) Positive (dashed line), negative (dotted line), and flux-balanced total flux divided by two (solid line) fluxes of the active region (AR) as a function of time from 2007 December 2 08:03 UT. The vertical dashed lines denote the time of onset of the two main flux cancellation events. The dot-dashed vertical line denotes the time at which a flux rope formed in the simulation. The dotted vertical line is the time of the observed B1.4-class *GOES* flare. Finally, the solid vertical line denotes the time after which we feel the magnetofrictional method can no longer be used to describe the evolution of the active region. (b) Flux imbalance of the active region as a function of time from 2007 December 2 08:03 UT before (solid line) and after (dot-dashed line) flux balancing.

the magnetograms, which make up the lower BC, must be in flux balance (see Appendix A).

To model the evolution of the AR, 120 cleaned magnetograms (see Appendix A for the cleaning process) taken at discrete intervals of 96 minutes are available, covering the eight-day period around central meridian passage. To run the simulation at a higher resolution than given in the magnetograms, the 127 × 127 grid-point magnetograms were interpolated onto a 256×256 grid. From these resulting magnetograms a continuous time sequence of lower boundary conditions is produced. This sequence of lower boundary conditions is designed to match each observed magnetogram, pixel by pixel, every 96 minutes. In order to model the evolution of the coronal field, A_{xb} and A_{yb}, the horizontal components of the vector potential **A** on the base that correspond to each magnetogram must be determined. This is carried out as follows.

1. Each of the observed magnetograms, $B_z(x, y, k)$, for $k = 1 \rightarrow 120$ are taken, where k represents the discrete 96 minute time index.

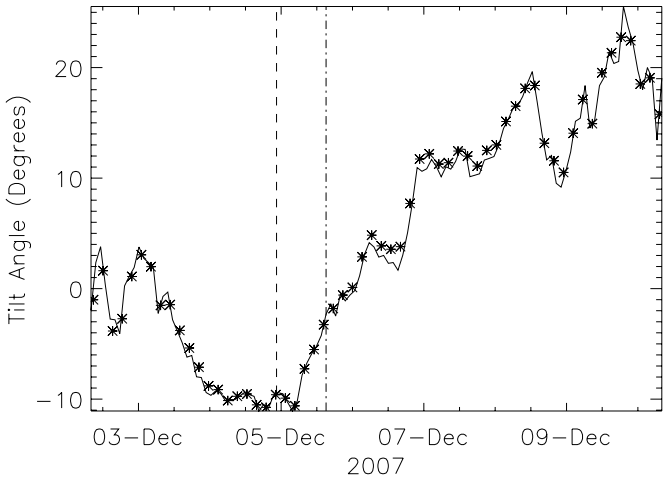

Figure 4. Tilt angle of the active region in degrees as a function of time from 2007 December 2 08:03 UT. The vertical dashed line denotes the time of onset of the first main flux cancellation event. The dot-dashed vertical line denotes the time at which a flux rope has formed in the simulation.

2. Next, the horizontal components of the vector potential at the base, $z = 0$, are written in the form

$$A_{xb}(x, y, k) = \frac{\partial \Phi}{\partial y},$$
$$A_{yb}(x, y, k) = -\frac{\partial \Phi}{\partial x},$$

   where Φ is a scalar potential.
3. For each discrete time index k, the equation

$$B_z = \frac{\partial A_{yb}}{\partial x} - \frac{\partial A_{xb}}{\partial y}$$

   then becomes

$$\frac{\partial^2 \Phi}{\partial x^2} + \frac{\partial^2 \Phi}{\partial y^2} = -B_z, \quad (5)$$

   which is solved using a multigrid numerical method. Details of this method can be found in the papers by Finn et al. (1994) and Longbottom (1998) and references therein.

Upon solving for the scalar potential, Φ, this determines the horizontal components of the vector potential on the base (A_{xb}, A_{yb}) for each discrete time interval, 96 minutes apart. To produce a continuous time sequence between each of the observed distributions, a linear interpolation of A_{xb} and A_{yb} between each time interval k and $k + 1$ is carried out. Between each observation, 500 interpolation steps are used. By linearly interpolating the horizontal components of the vector potential on the base, this effectively evolves the magnetic field from one state to the other. Numerically, it also means that undesirable effects such as numerical overshoot or flux pile up at cancellation sites do not occur and no additional numerical techniques to remove these are required.

The technique described above means that there are two time scales involved in the evolution of the lower boundary condition. The first, which is 96 minutes, is the time scale between observations, the second which is 11.52s is the time scale introduced to produce the advection of the magnetic polarities between observed states by interpolation, along with the relaxation of the coronal field. The process described above

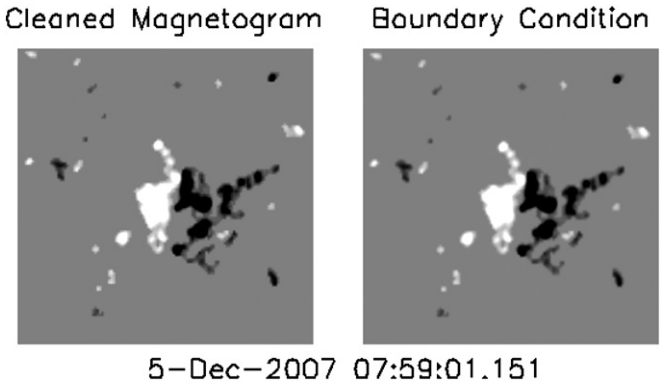

Figure 5. Comparison of a cleaned magnetogram (left) and the corresponding lower boundary condition used within the simulation (right) at 07:59:01 UT on 2007 December 5. The images saturate at ±100 G.

(An animation of this figure is available in the online journal.)

reproduces the observed magnetograms at each 96 minute discrete time interval and therefore produces a highly accurate description of the magnetogram observations and the life of the AR.

Figure 5 displays a comparison of the cleaned magnetogram (left) and the normal magnetic field component used as the lower boundary condition in the simulation (right) at 07:59 UT on 2007 December 5. A good agreement between the two is found. A movie comparing the full time series can be viewed in movie1.mpg in the online journal. At this point, it should be noted that the above technique only specifies A_{xb}, A_{yb} at $z = 0$. However, it does not specify A_z, which lies one-half of a grid point up and is determined by Equation (1), the coronal evolution equation. Non-potential effects near the base, as a result of the evolving lower boundary condition, may be contained within this term. This results in a continuous sequence of non-potential coronal fields that evolve due to the changing photospheric field.

An initial coronal field for the AR must now be prescribed. This is extrapolated from the first cleaned LOS magnetogram frame corresponding to 08:03 UT on 2007 December 2 on a grid of 256^3 cells. The sides of the cube range from $0 < x, y, z < 6$ in non-dimensionalized units, where one unit in length is equal to 30,352 km on the Sun. The method used to produce the initial condition is described in Finn et al. (1994) and for further details see Mackay et al. (2011). Since no vector magnetic field data is available to constrain the initial condition, a potential field is used. Although unique, a potential field has the limitation that no electric current systems exist within it, and correspondingly it is the field of lowest energy for any given boundary conditions. It should be noted that while we use a potential field for the initial condition, we do not expect the field of the AR to be potential at this time. Due to this, additional simulations have also been run using LFF fields. The consequences of varying the initial condition will be discussed in the conclusions. Figure 6 shows the potential field initial condition corresponding to 08:03 UT on 2007 December 2 where red contours represent positive flux and blue contours represent negative flux.

5. RESULTS

5.1. Magnetic Field Line Evolution

We now describe the evolution of the coronal field in the simulation. To describe sheared field lines across the PIL, first we define the shear of the field. The shear is defined relative to the normal of the PIL. Consider a field line that has a component

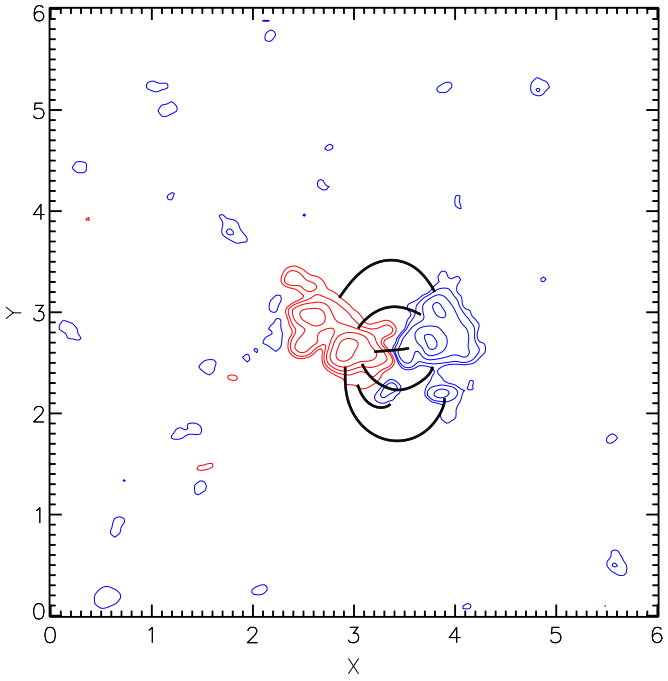

Figure 6. Selection of field lines (solid black lines) illustrating the potential field initial condition where red contours denote positive flux and blue contours denote negative flux of the photospheric magnetic field, respectively.

(A color version of this figure is available in the online journal.)

that lies parallel to the PIL. When viewed from the positive polarity side of the PIL, if the component parallel to the PIL is directed to the left (right), then the field line is defined to have sinistral (dextral) shear.

Figure 7 displays a selection of field line plots from the simulation, at times approximately corresponding to the XRT observations presented in Figure 2. The field lines plotted in Figure 7 highlight the features observed by XRT that are reproduced by the simulation. In the top left panel of Figure 7—corresponding to the top left panel of Figure 2—an arcade field is visible in the simulation at the same location as the observed XRT arcade field. While this shows good agreement, the simulated field has almost no shear while the observed field has a slight sinistral shear. This difference is most likely due to the potential initial condition. The curved J-shaped arcade field in the south of the field line plot is in good agreement with the faint J-shaped emission in the XRT observation. In the top right panel of Figure 7—corresponding to the top right panel of Figure 2—an FR with S-shaped field lines as seen in projection has formed at the location of the strongly sheared field observed by XRT. The extent of the simulated FR is in very good agreement with the extent of the observed emission. The arcade field lines in the south of the AR match well with the arcade-like emission in the XRT observations. The curved field lines in the north of the AR also match with the faint loops in the XRT observations. In the bottom left panel of Figure 7—corresponding to the bottom left panel of Figure 2—the S-shaped field lines are clearly visible at the location of the observed sigmoid. The northern half of the sigmoid is very well described by the simulation; however, the southern half of the FR terminates further north than the observed sigmoid. Arcade field lines are present in the south of the AR as is seen in the observations. The simulated arcade agrees relatively well with the observed arcade. One difference between the simulated and observed arcade is that

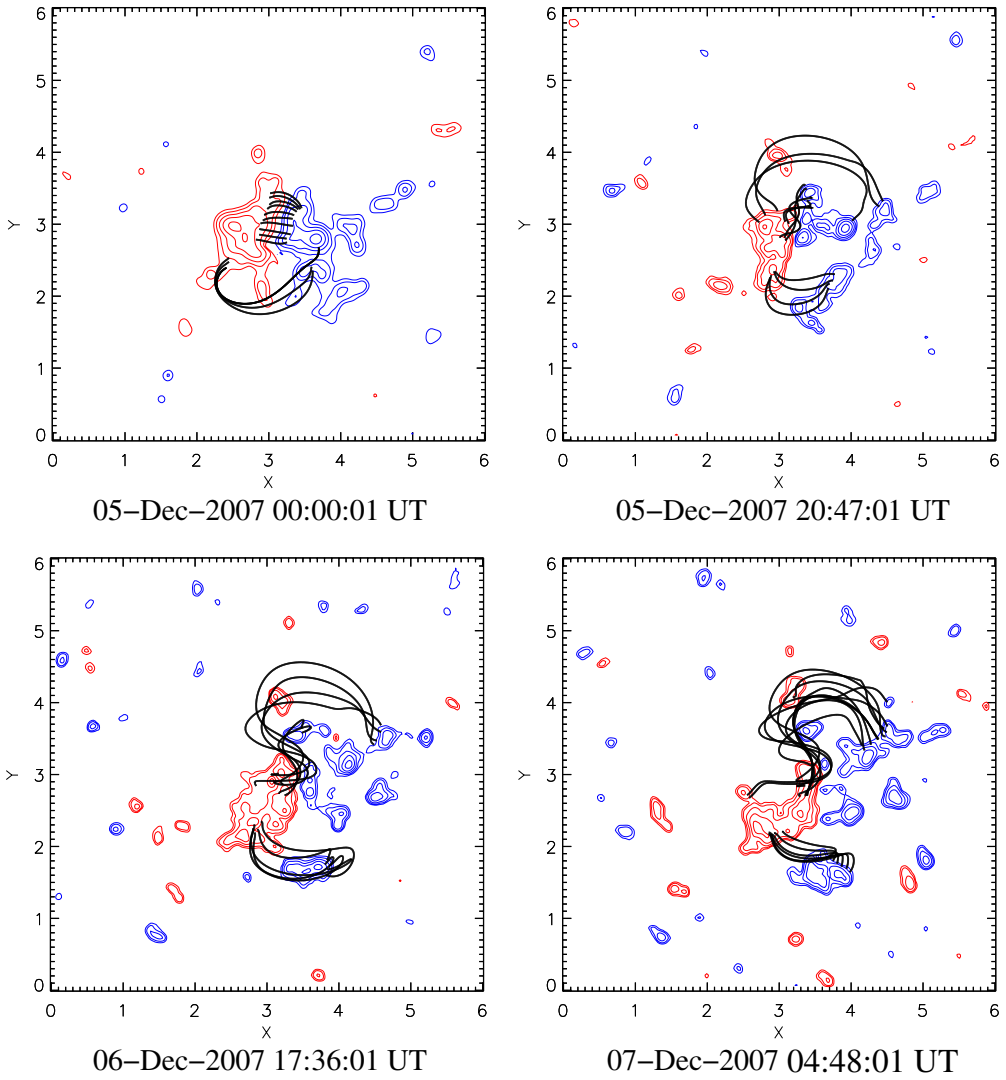

Figure 7. Field line plots generated from the simulation at various times approximately corresponding to the times in Figure 2. The red and blue contours denote the positive and negative photospheric fields, respectively.

(A color version of this figure is available in the online journal.)

the footpoints of the arcade in the negative polarity region in the simulation are on the leading (relative to rotation) side of the flux fragment, while in the observations the footpoints appear to be on the trailing side of the flux fragment. In the bottom right panel of Figure 7—corresponding to the bottom right panel of Figure 2—the S-shaped field lines belonging to the FR have increased in length, resulting in a larger S-shaped feature. This is also seen in the XRT observations. While in the XRT observations the southern footpoint of the sigmoid has extended further south, in the simulation the southern footpoints of the FR have extended further west (to the left in Figure 7). The arcade in the south of the AR present in the observations is also visible in the field line plot, and is in general agreement with the observed arcade. It can be seen that all the panels of Figure 7 are in good agreement with the observations. This agreement illustrates that by employing a continuous time-evolution of the coronal field, driven through observed LOS magnetograms, the model of Mackay et al. (2011) can qualitatively capture observed features of the AR, particularly the sheared (non-potential) components. The agreement is especially strong at the northern end of the FR present in the top-left and bottom panels. The agreement is not so good in the southern part of the FR. This is attributed to the initial condition coronal field chosen. The consequences of varying the initial condition are discussed in Section 6.

The formation of the FR present in the top right and bottom panels of Figure 7 is now described in detail. In the simulation, the FR had formed by 14:23 UT on 2007 December 5 (this time is denoted by a dot-dash vertical line in Figures 3(a), 4, and 11). Figure 8 outlines the formation of the FR field lines. In Figure 8(a), two sheared arcade field lines can be seen. As a result of the convergence of the positive and negative magnetic polarities—leading to flux cancellation—the footpoints are advected toward the PIL. Reconnection occurs at the PIL, producing a long, helical field line (Figure 8(b)), and a small loop, which was then removed by the flux cancellation. This is in agreement with the FR formation mechanism proposed by van Ballegooijen & Martens (1989). In the XRT observations, the sigmoid was not observed until just over a day later at 15:51 UT on 2007 December 6. This indicates that there is not a simple relationship between the formation of an FR as expressed in terms of magnetic field lines and the observation of a sigmoid

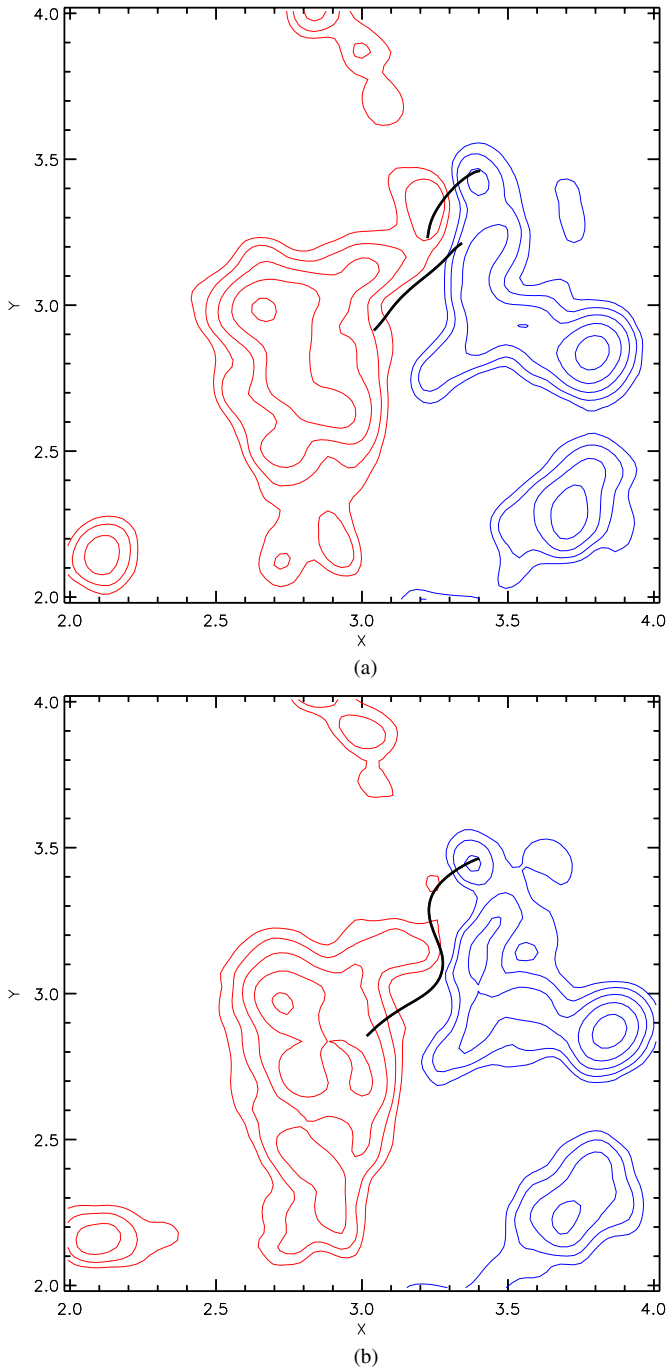

Figure 8. Formation of the flux rope. (a) The sheared arcade is advected toward the polarity inversion line (PIL). (b) Reconnection occurs between the northerly footpoint of the southern field line, and the southerly footpoint of the northerly field line, producing a long helical field line and a short field line which is removed by flux cancellation. Panels (a) and (b) correspond to 09:35 UT and 14:23 UT on 2007 December 5, respectively. The red and blue contours denote the positive and negative photospheric field, respectively.

(A color version of this figure is available in the online journal.)

seen in X-rays. The difference in times between the two can also be related to the initial condition used in the simulation.

By the fifth day of the simulation (2007 December 7, 09:36 UT), the field lines have become strongly twisted and the magnetofrictional method can no longer properly describe the coronal evolution. The simulation's results are therefore not to be trusted after the fifth day (denoted by a solid vertical line in Figures 3(a) and 11). It is interesting to note that this time is just

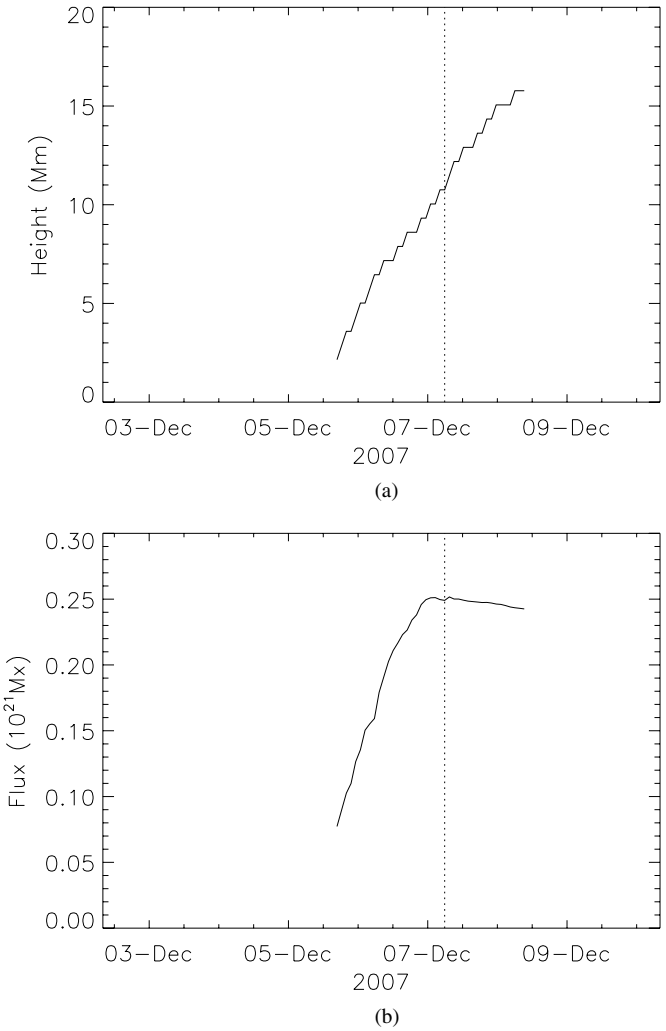

Figure 9. Evolution of (a) the height and (b) flux of the FR with time from 08:03 UT on 2007 December 2. The vertical dotted line denotes the time of the flare observed by XRT.

after the occurrence of a flare which was observed at 04:20 UT on 2007 December 7 and is indicated by a vertical dotted line in Figures 3(a), 9, and 11. This indicates that the build-up phase to eruption has been successfully followed in the simulation. To follow the dynamics of the eruption, a full MHD simulation would have to be run (Pagano et al. 2013).

5.2. Flux Rope Properties

The flux content within the FR and its height are calculated. To compute these quantities, a cut of B_y in the x–z plane centered at $y = 3.4$ is taken. This y coordinate approximates the location of the mid-point of the FR axis throughout the duration of the simulation. The location (x_0, z_0) of the maximum of B_y in the cut is determined. From this the height of the FR from the photosphere is defined as z_0. Figure 9(a) displays the height of the FR with time. It shows a near linear increase, implying that the FR was rising at almost constant velocity, calculated to be 63 m s^{-1}. The center of the FR reached a height of 11 Mm by the time of the observed flare (dotted line in Figure 9(a)).

In order to calculate the flux contained within the FR, first the FWHM of the peak of B_y about (x_0, z_0) in the cut is determined.

This is found in the x-direction by determining the points x_1 and x_2 on either side of the maximum, x_0, where B_y decreases to one half of the value at x_0. The FWHM is then calculated by $r_{\rm FWHM} = |(x_1 - x_2)|/2$ and the flux of the FR is calculated by integrating B_y within a circle of radius $4r_{\rm FWHM}$ centered around the point of maximum B_y. Upon investigating various radii of circles to determine the flux in the FR, it was found that the vast majority of the FR flux was contained within a radius of $4r_{\rm FWHM}$. This was thus chosen as the radius of the circle through which the flux values quoted in this study are determined.

Figure 9(b) shows the evolution of the FR's flux with time. The flux initially increases almost linearly with time, then levels off at around 2.5×10^{20} Mx. The increase in the flux corresponds to the flux cancellation event at the center of the AR where axial flux is built into the FR. It should be noted that although the flux contained within the FR levels off, flux cancellation still occurs in the AR. This flux cancellation, however, does not act to build additional flux into the FR as it occurs at a different location. At the time of the first flare (denoted by the dotted line in Figure 9(b)), the flux within the FR is approximately 20% of the AR flux at that time. This value is lower than the values obtained by Green et al. (2011) and Savcheva et al. (2012). It should be noted that although Savcheva et al. (2012) obtained the FR flux to be roughly 50% of the AR flux, this quantity was calculated from the flux in the inserted FR at the time of insertion. During the relaxation, it is possible that some of the FR flux may have reconnected with surrounding fields, and no longer belonged to the FR. Thus their estimate of 50% may be regarded as an upper limit.

The critical ratio of FR flux to AR flux in order for an FR to remain stable was found to be 10%–14% by Bobra et al. (2008), Su et al. (2009), and Savcheva & van Ballegooijen (2009). Interestingly, using this stability criterion, the FR in our simulation, which contains 20% of the AR flux at the time of the observed flare, is expected to be unstable. The FR to AR flux ratio of 50% determined by Savcheva et al. (2012) is much higher than the 10%–14% found by Bobra et al. (2008), Su et al. (2009), and Savcheva & van Ballegooijen (2009), and much higher than the ratio obtained in the present study. We note that the ratio determined by Savcheva et al. (2012) is inconsistent with the studies that find 10%–14%. The reason for this is presently unclear, but will need to be investigated in the future.

5.3. Comparison to XRT Images

We now compare the simulation results to the XRT images through computing a simple representation of the XRT images. This representation is achieved by assuming that the emission in the XRT images is due to Ohmic heating, which is proportional to j^2. To produce a j^2 emission proxy of XRT images, the square of the current density is calculated at all points within the simulation and integrated along the z direction. By doing so, we calculate the emission proxy in the same manner as Meyer et al. (2013a). It should be noted that Cheung & DeRosa (2012) carried out a similar approach for calculating an emission proxy, however, they determined the mean current density along field lines and used this to compute the proxy image. It should also be noted that X-ray emission can only be calculated accurately from a full MHD simulation, as the emission is dependent upon a number of effects, such as density, temperature, and thermal conduction. This is, however, beyond the scope of the present study and therefore we use the simpler j^2 emission proxy. For a discussion on the limitations of emission proxies derived solely from the current density, we direct the reader to Section 2.4 of Cheung & DeRosa (2012).

Figure 10 displays the LOS integrated j^2 emission proxy for times approximately equal to those of the XRT observations presented in Figure 2. The top left panel of Figure 10, corresponding to the top left panel of Figure 2, displays strong j^2 proxy emission in the north of the AR, the same location as strong emission observed by XRT. Strong j^2 proxy emission is also present at the south of the AR, which is not visible in the XRT image. The C-shaped feature to the west of the AR is an FR formed due to boundary effects, and is unphysical. This is also faintly visible in the other panels of Figure 10. The top right panel of Figure 10, corresponding to the top right panel of Figure 2, again possesses strong j^2 proxy emission at the north of the AR in good agreement with the XRT observations; however, the j^2 emission proxy feature in the south bears little resemblance to the emission observed in the south by XRT. The bottom left panel of Figure 10, corresponding to the bottom left panel of Figure 2, has strong j^2 proxy emission at the same location as the observed sigmoid. The j^2 emission proxy image reproduces the observed emission at the northern end of the sigmoid well, but is not so good at reproducing the emission at the south of the sigmoid as the j^2 proxy emission stops further north than that seen in the XRT observation. The arcade emission visible in the south of the XRT observation is not present in the j^2 emission proxy image. The bottom right panel of Figure 10, corresponding to the bottom right panel of Figure 2, displays a j^2 emission proxy map very similar to that of the bottom left panel. The excess j^2 proxy emission in the south of the AR visible in every panel is due to a second FR formed in the simulation. The FR has the opposite direction of twist to that found in the northern FR, and its origins will be discussed in Section 6.

While the LOS integrated j^2 emission proxy images have reproduced emission at the position of the sigmoid relatively well, they have been unable to reproduce the arcade seen in the observed XRT images. This may be due to the crude method employed. Additionally, in the j^2 emission proxy images, only the center of the FR can be seen. This can be explained by the field within the volume of the FR being twisted, and thus containing current. This would translate into more emission in our j^2 emission proxy images. In the Titov & Démoulin (1999) model, the emission responsible for sigmoids is generated in a thin current layer underneath the FR. In our j^2 emission proxy images, this thin layer will have the "emission" from the current within the FR superimposed on top of it and will likely not be discernible in the images.

5.4. Free Magnetic Energy

Following the methodology of Mackay et al. (2011), we now investigate the evolution of free magnetic energy in the simulation. The free magnetic energy is defined as

$$E = \frac{1}{8\pi} \int \left(B^2 - B_p^2\right) d\tau, \tag{6}$$

where B is the magnetic flux density from the simulation, and B_p is the magnetic flux density corresponding to a potential field extrapolated from the same boundary conditions as the simulation field. The potential fields are calculated in the same way as the initial condition potential field. Figure 11 shows the time-evolution of the free magnetic energy for the simulation. The sharp rise of the free magnetic energy around the start of 2007 December 5 corresponds to the first large flux cancellation

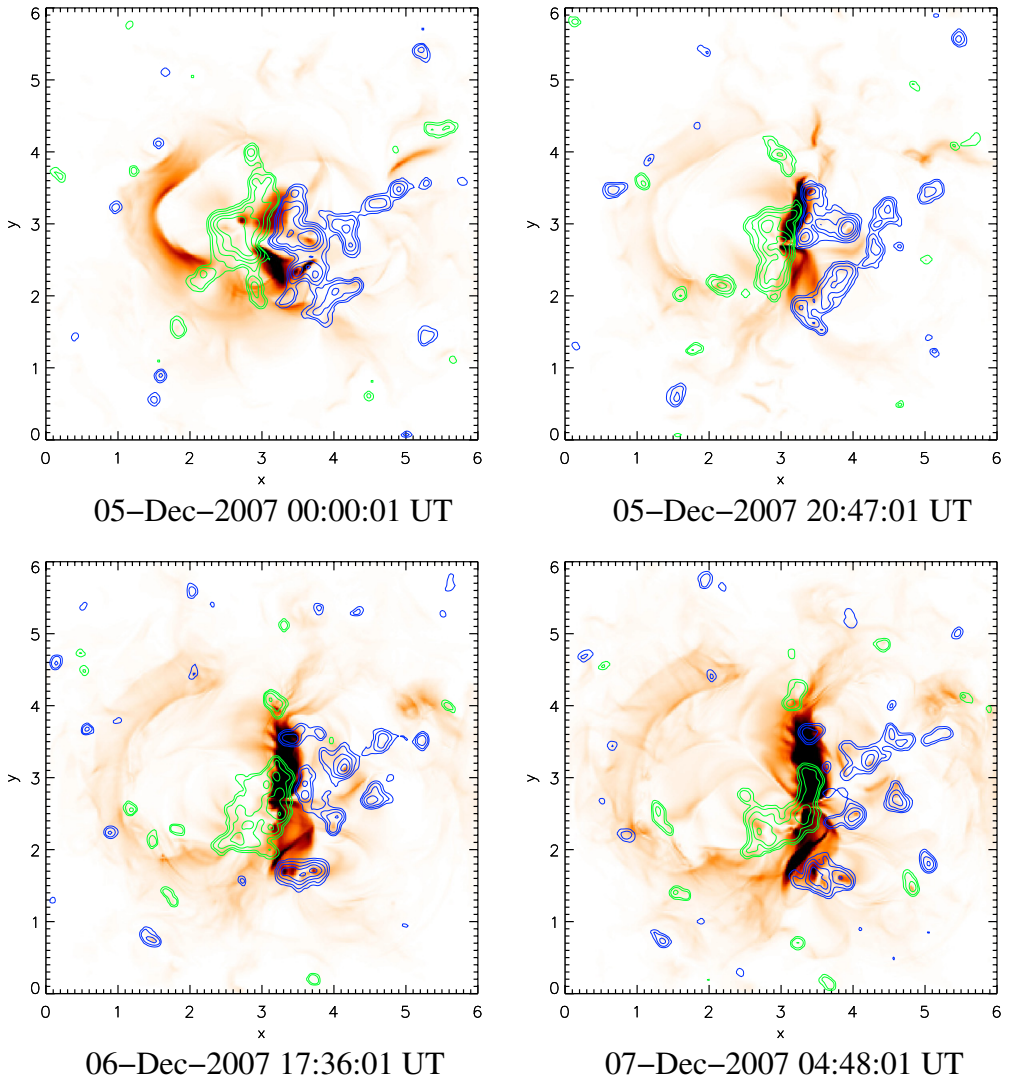

Figure 10. j^2 emission proxy images generated from the simulation at various times roughly corresponding to the times in Figure 2. The images display a strong j^2 proxy emission in the same location as the observed sigmoid. The color scaling saturates at one-quarter of the maximum value of the LOS integrated j^2 for each image. (A color version of this figure is available in the online journal.)

event (denoted by the dashed vertical line in Figure 11) and the CCW shearing motions. The FR was formed during this process (denoted by the dot-dashed line in Figure 11). This suggests that much of the free magnetic energy is stored within the FR. Indeed, a plot of the free magnetic energy density integrated along the z-axis—Figure 12—reveals that the majority of the free magnetic energy (white region) is stored at the location of the FR. The free magnetic energy contained within the FR is calculated at 04:48 UT on 2007 December 7 to be 3.9×10^{30} erg. This is more than sufficient to account for a B-class *GOES* flare, which is estimated to emit $\gtrsim 10^{27}$ erg (Hannah et al. 2011). The free energy of the FR is in general agreement with the values found in Savcheva et al. (2012), who found a free energy of 6×10^{30} erg contained within the FR in their simulations.

5.5. Helicity

Motions at the photosphere inject magnetic helicity in addition to free magnetic energy into the corona. Helicity is a topological measure of the connectivity of the magnetic field, and is invariant in ideal MHD, and approximately conserved during magnetic reconnection (Berger 1999). Here we investigate the evolution of the relative helicity in our simulation in a manner consistent with Mackay et al. (2011). The relative helicity, which is gauge invariant, is calculated by

$$H_r = \int (\mathbf{A} \cdot \mathbf{B}) d\tau - \int (\mathbf{A}_p \cdot \mathbf{B}_p) d\tau, \quad (7)$$

where $\mathbf{A}$ is the magnetic vector potential for the simulation's magnetic flux density, $\mathbf{B}$, and $\mathbf{A}_p$ is the magnetic vector potential for the potential field, $\mathbf{B}_p$, corresponding to the same photospheric field and BCs. Figure 13 displays the time evolution of the relative helicity for the simulation.

In Figure 13, the relative helicity initially decreases until the beginning of December 4, then increases almost linearly for the remainder of the simulation. This is qualitatively similar to the evolution of the tilt angle of the AR (Figure 4), which initially decreases until December 4, remains constant for just over one day, then increases for the duration of the observations. With the exception of the first two days of the simulation, the general trend in the relative helicity is a linear increase, implying the near constant injection of positive helicity into the corona. This is in agreement with previous studies which show that the

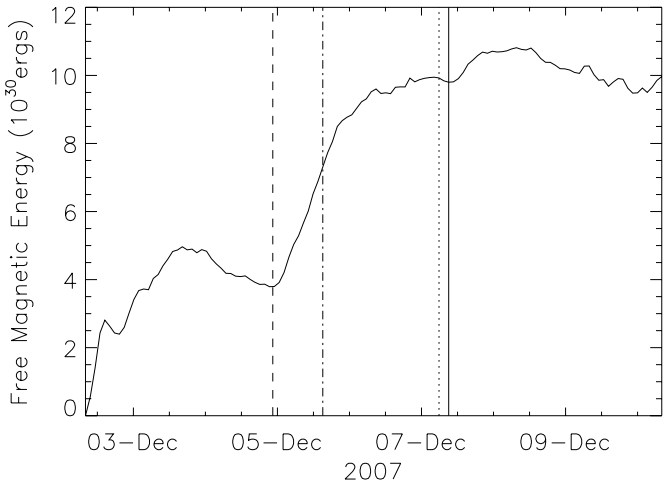

Figure 11. Free magnetic energy as a function of time from 08:03 UT on 2007 December 2. Note the sharp rise in free magnetic energy beginning late on December 4. This corresponds to the time of the initial flux cancellation event and formation of the FR. The vertical dashed line denotes the time of onset of the main flux cancellation event. The dot-dashed vertical line denotes the time at which a flux rope has formed in the simulation. The dotted vertical line is the time of the observed B1.4-class *GOES* flare. Finally, the solid vertical line denotes the time after which we feel the magnetofrictional method can no longer be used to describe the evolution of the active region.

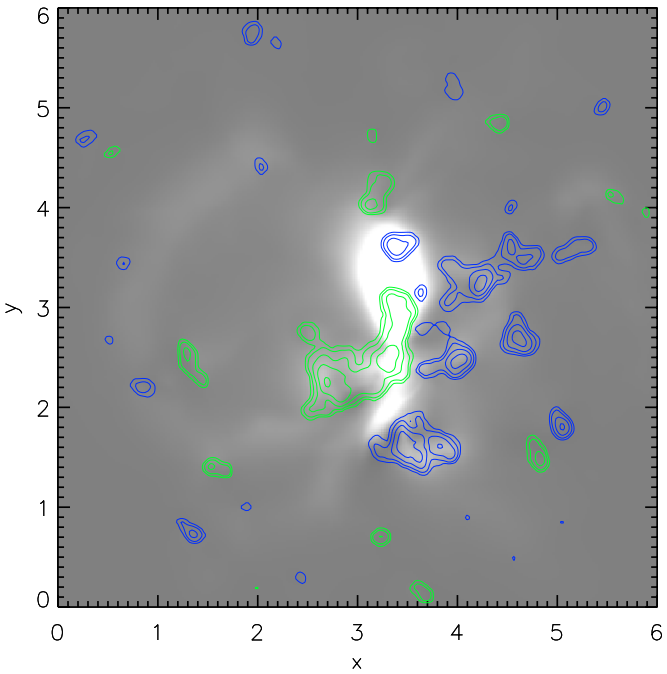

Figure 12. Integral of the free magnetic energy density along the z-axis at 04:48 UT on 2007 December 7, where white denotes areas of high free magnetic energy storage and gray denote areas of low free magnetic energy storage.

(A color version of this figure is available in the online journal.)

dominant sign of helicity in southern hemisphere ARs is positive (Pevtsov et al. 1995). The qualitative temporal evolution of the tilt angle (Figure 4) is very similar to the temporal evolution of the helicity (Figure 13). This suggests that the dominant source of helicity injection is the large-scale rotation of the AR. This is in agreement with Mackay et al. (2011), who proposed that the increase of helicity in their simulation may be related to the evolution of the large scale properties of their AR. While the large scale evolution of the AR is one source of helicity injection, other sources may also exist. Section 4.3 of Mackay

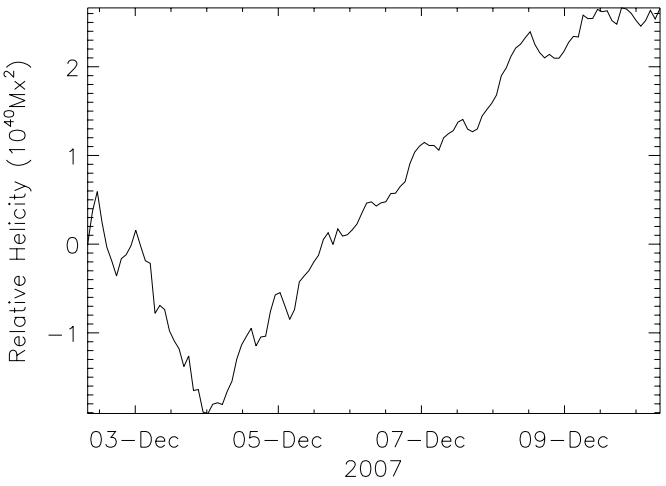

Figure 13. Relative helicity as a function of time from 08:03 UT on 2007 December 2.

et al. (2011) presents a discussion on other possible sources of helicity injection. Savcheva et al. (2012) find a helicity of 3×10^{41} Mx^2, which is roughly a factor of 10 greater than the value obtained in this paper. It must be noted, however, that the volume over which the relative helicity in Savcheva et al. (2012) was calculated may not have been the same as the volume integrated in our simulation, and thus the two values may not be directly compared.

6. DISCUSSION AND CONCLUSIONS

In the present study, we have simulated the coronal magnetic field of AR10977 from its initial emergence phase, followed by a decay phase with significant flux cancellation and CCW rotation. X-ray observations of the AR showed that a sigmoid formed during its lifetime and eventually led to an eruption from the AR. To simulate these events, the coronal magnetic field of the AR was modeled using the method of Mackay et al. (2011), where its evolution was driven by a series of 96 minute LOS magnetograms from *SOHO*/MDI. These magnetograms produced an evolving lower boundary condition closely resembling that observed.

By applying this technique—which provides the first continuous time evolution of AR10977—the main features of the evolution of the AR's coronal magnetic field as observed by *Hinode*/XRT were reproduced. This verifies that the modeling technique of using LOS magnetograms put forward by Mackay et al. (2011), but not previously tested against coronal observations, is a valid technique to study the evolution of the coronal magnetic field. In particular, in the simulation, an FR formed on 2007 December 5, whose location matched the location of a *Hinode*/XRT sigmoid. In the present study, we determined the formation mechanism of the FR and investigated its properties. The FR formed as a result of the transformation of a sheared arcade into twisted field lines due to flux cancellation. This was in agreement with the FR formation method proposed by van Ballegooijen & Martens (1989). The shear of the arcade originated from the CCW rotation of the negative magnetic polarity region relative to the positive polarity region. The FR continued to increase in size until the time of the observed eruption, where analysis of the FR determined that it contained 2.5×10^{20} Mx of flux. This is approximately 20% of the AR flux, which is lower than the results found in Green et al. (2011) and Savcheva et al. (2012); however, it is just greater than the critical ratio

for force balance found in previous studies (Bobra et al. 2008; Su et al. 2009; Savcheva & van Ballegooijen 2009), suggesting that the FR was unstable at the time of the observed flare. The FR was also found to be rising with a constant velocity of 63 m s^{-1}. In general, comparisons of the field lines from the simulation with the XRT observations showed a good agreement, with the simulation reproducing many of the observed features. The simulation provided a very good fit for the northern half of the FR; however, the fit was not so good for the southern end of the FR. In order to directly compare our simulated coronal field with XRT observations, j^2 emission proxy images were produced by integrating the square of the current density along the z direction. These images again showed that our simulation better reproduced the observed features in the north of the AR compared to the south.

The free magnetic energy was calculated as a function of time for the simulation. Over the duration of the simulation, approximately 1×10^{31} erg of free magnetic energy was injected into the corona. There was a sharp rise in the free magnetic energy beginning early on 2007 December 5. This time corresponded to a large flux cancellation event and the FR formation, suggesting that much of the free magnetic energy input is associated with the FR formation. The free magnetic energy contained within the FR at the time of the flare was found to be 3.9×10^{30} erg. This is in good agreement with the results of Savcheva et al. (2012), who found an energy of 6×10^{30} erg. It should be noted here that the value of the free magnetic energy quoted in Savcheva et al. (2012) was determined after their FR had relaxed, in contrast to their quoted flux values for their FR, which were determined prior to the relaxation. This means that a useful comparison with our results may only be made with the free magnetic energy quoted in Savcheva et al. (2012).

The relative helicity, a topological measure of the connectivity of the magnetic field, was calculated as a function of time for the simulation. The relative helicity initially decreased, but later increased for the duration of the simulation. The evolution of the relative helicity with time is correlated with the evolution of the tilt angle of the AR. This suggests that the rotation of the AR is a significant source of net helicity injection into the corona.

In the simulation, a second FR formed to the south of the FR associated with the observed sigmoid. This additional FR formed when the negative polarity region in the magnetograms first began to fragment, and a portion of it moved southward (top center and top right panel of Figure 1), producing an arcade with a strong dextral shear. This FR possessed the opposite direction of twist compared to the FR associated with the observed sigmoid. Due to this, its soft X-ray signature would be a sigmoid with an inverted S-shape. In the XRT observations (Figure 2) there is no such inverted S-shaped feature present in the southern portion of the AR.

We now investigate the origin of this discrepancy in terms of the arbitrary choice of the initial condition. One possibility is that the initial condition used in the simulation was incorrect at this location. If the initial condition possessed a shear across the PIL of a sinistral type (positive relative helicity), then during the initial fragmentation of the negative polarity region no arcade with dextral shear would form at the south of the AR, preventing the formation of the southern FR. Such an initial condition field with sinistral shear would possess a positive relative helicity. This would result in a value of relative helicity that is closer to that found by Savcheva et al. (2012) compared to the value obtained from the potential field initial condition.

Additional simulations with LFF initial conditions were carried out. Simulations with negative and positive force-free parameters, α, were used. The simulation with a positive α (corresponding to an initial sinistral shear across the PIL) better reproduced the observations at the south of the AR compared to the simulation with the potential initial condition. In contrast, the simulation with negative α resulted in a much worse fit. A drawback of the simulation with positive α, however, is that it produced a worse fit in the northern part of the AR compared to the simulation described in the paper. From this it can be deduced that the best agreement with the observations may occur from a non-linear force-free field initial condition with $\alpha = 0$ in the northern part of the AR and $\alpha > 0$ in the southern part. The production of such an initial condition is beyond the scope of the present paper. In future studies, vector data from *SDO*/HMI should be used to better constrain the initial condition.

In a previous study, Cheung & DeRosa (2012) model a different AR using the magnetofrictional method in a manner very similar to that of Mackay et al. (2011) and this present paper. In their study, they are able to form an FR in the AR by imposing an unobserved spatially uniform twisting motion to their lower boundary conditions. Interestingly, in the present study, we do not need to impose any such twisting motions in order to form the FR at the location of the XRT sigmoid. It is presently unclear why our model of the AR does not require the extra twisting motions. Two possible explanations are that either: (1) the evolution of the magnetic field of the AR considered here is fundamentally different compared to the one studied by Cheung & DeRosa (2012). A detailed study of the magnetic evolution of the two ARs would be required to determine if this is the case. (2) The boundary treatments of Cheung & DeRosa (2012) and Mackay et al. (2011) may inject different non-potential fields into the corona. It is possible that the technique used in the present study captures a horizontal non-potential component that builds up the axial flux of the FR. In contrast, Cheung & DeRosa (2012) may require the inclusion of twisting motions if their technique injects a weaker non-potential horizontal component. Resolving these issues is beyond the scope of the present paper, but will be considered in a future study.

On the morning of December 7, the simulation's field lines became too twisted for the magnetofrictional method to remain valid. This time lies within a few hours of the eruption of the sigmoid. The loss of validity of the magnetofrictional method, which evolves a field through a series of NLFF equilibria, is a suggestion that an instability or non-equilibrium state has occurred, which the simulation cannot track. It should be noted that the choice of the magnetofrictional coefficient affects the timescale over which the coronal field can respond to changes produced by the photospheric evolution. This process and its corresponding timescales are comprehensively discussed in Section 2.1 of Cheung & DeRosa (2012). Our choice of large frictional coefficient, although ensuring that the simulated field remains close to an NLFF configuration at all times, results in long evolution timescales. In our study, the FR does not erupt, although the simulation breaks down soon after the time of the observed flare. This is an indication that the coronal field is attempting to evolve faster than the magnetofrictional code—with our choice of frictional coefficient—can deal with. This implies a loss of equilibrium has occurred. It is interesting that the time of the flare and the time of the breakdown in the simulation occur within a few hours of one another. This suggests that the simulation technique of using observed

magnetograms to drive the evolution of the coronal field has correctly followed the dynamics of the system to the build-up of an eruption.

In the present study, we have tested the modeling technique of Mackay et al. (2011), which uses a time series of Michelson Doppler Imager (MDI) magnetograms and a magnetofrictional relaxation technique. The test, which produces results consistent with a previous observational study (Green et al. 2011) and static models (Savcheva et al. 2012) is also able to successfully reproduce the time-evolution of the AR as observed by *Hinode*/XRT. These included the formation of a sigmoidal FR through flux cancellation and the development of the FR toward eruption. In particular, we find that twisting motions such as those employed by Cheung & DeRosa (2012) to match coronal images are not required. In addition, the technique we applied shows that solely surface motions deduced from observed magnetograms can be sufficient to explain the energy required to satisfy the observed flare. This study shows that magnetofrictional techniques driven by observed LOS magnetograms—such as those of Mackay et al. (2011)—are a very useful tool with which to study the evolution of the solar corona.

G.P.S.G. would like to thank the STFC for financial support. D.H.M. would like to thank the STFC, the Leverhulme Trust, and the EU FP7 funded project "SWIFF" (263340) for financial support. L.M.G. is grateful to the Royal Society for a University Research Fellowship. K.A.M. thanks the Leverhulme Trust for financial support. Simulations were carried out on a STFC/SRIF funded UKMHD cluster at St Andrews.

APPENDIX A

MAGNETOGRAM CLEAN-UP

The magnetograms used in this study were taken by the MDI on board the *Solar and Heliospheric Observatory* (*SOHO*) spacecraft. Each magnetogram provides the LOS magnetic flux density (Mx cm^{-2}). In total, 129 full disk magnetograms are used, each with a spatial resolution of 1.″97790 pixel^{-1} and cadence of 96 minutes. The first observation is at 00:03 UT on 2007 December 2, while the final observation is at 22:23 UT on 2007 December 10. Each full disk magnetogram was de-rotated so that AR10977—which was in the southern hemisphere of the Sun—lies at disk center. Following this, each magnetogram was corrected for LOS effects so that each pixel corresponded to the component of magnetic flux density normal to the photosphere. From the de-rotated and corrected images a 127 × 127 pixel image was extracted centered on the AR.

It is clear from Figure 1 that significant noise exists in the magnetogram frames over all times, but this is especially true in the early and late frames (e.g., the top left and bottom right frames of Figure 1) where the AR was close to the limb of the Sun. In order to reduce the noise so that the magnetograms can be used as boundary conditions in the simulation, several cleanup procedures were applied. First, noise was reduced by time-averaging the frames with a Gaussian kernel. This was achieved by applying the following operation:

$$C_i = \frac{\sum_{j=1}^{129} \exp(-([i-j]/\tau)^2) F_j}{\sum_{j=1}^{129} \exp(-([i-j]/\tau)^2)}, \quad \text{(A1)}$$

where C_i is the ith cleaned frame, with i ranging from 1–129, F_j is the jth raw frame, and τ is the separation of frames where the weighting falls by $1/e$. For the present data we set the separation to be $\tau = 2$ frames. Each cleaned frame is thus a linear combination of the 129 raw frames, but where the two frames before and two frames after have the highest weighting. The procedure was effective in removing the random noise present but retained the large magnetic features. After the noise reduction was applied, the cleaned frames numbered 1–5 and 125–129 were discarded as at these times the AR was very close to the limb of the Sun and thus the frames still remained very noisy. Also, the time averaging was less effective for the first and last frames as the cleaned frames were composed from a one-sided averaging process.

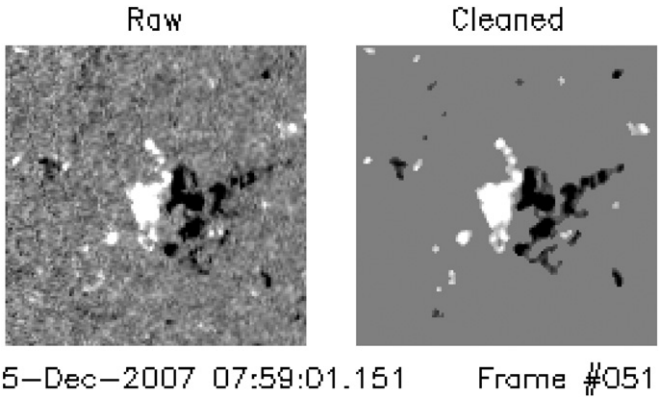

Figure 14. Comparison of a raw and cleaned magnetogram frame of observations taken at 07:59:01 UT on 2007 December 5. The field strength is set to saturate at ±100 G in both frames.

(An animation of this figure is available in the online journal.)

As well as removing the noise, small isolated magnetic flux features were removed since in the present study we are interested in the large-scale evolution of the AR and not the small scale features such as network magnetic elements found at the boundaries of super-granular cells. This was achieved on a pixel-by-pixel basis, where for each pixel its eight neighbors were considered. If fewer than four of its neighbors had the same sign of flux, then that pixel's value was set to zero. Pixels along the edges of the magnetograms—that had fewer that eight neighbors—had their values set to zero. Additionally, pixels with absolute values of less than 25 Mx cm^{-2} were set to zero in the cleaned magnetograms. This was motivated by histograms of the absolute values of the pixels of each frame, which were flat for values of less than roughly 25 Mx cm^{-2}. These low fluxes were interpreted to be background flux values, related to the "quiet" regions around the AR.

Finally, each magnetogram frame was adjusted so that it was in exact flux balance. This is required for the simulation (see Section 4 for details). Flux balance was achieved by calculating the signed flux of each frame. For each frame the number of non-zero-valued pixels was counted, and the signed flux was then divided by this number. Finally, the imbalanced flux per non-zero valued pixel was subtracted from every non-zero valued pixel. This method ensured that pixels that initially had zero flux, remained at zero flux and adjusted every non-zero valued pixel equally. The mean correction per pixel was 8 Mx cm^{-2}, with a maximum correction of 17 Mx cm^{-2}. Since at an earlier stage all pixels with absolute values of flux density lower than 25 Mx cm^{-2} were set to zero, no pixels changed sign during the flux balancing procedure.

Figure 14 gives a comparison of a single raw and cleaned magnetogram frame, taken at 07:59:01 UT on 2007 December 5. It is clear from comparing the two images that the shape and

strength of the main magnetic flux features are still present while the noise and small-scale elements are removed. A movie comparing the entire data set of raw and cleaned images can be seen in the online journal.

In this study, we have applied several cleanup procedures, namely, time averaging, removal of isolated features, removal of low flux values, and flux balancing. This is in contrast to Mackay et al. (2011), who only carried out the flux balancing necessary for the magnetograms to be used as a lower boundary condition in their simulation. The motivations for carrying out the additional cleanup procedures in this study are as follows. First, AR10977 was close to the limb of the sun at the beginning and end of the observations, resulting in the de-rotated magnetograms being very noisy at these times. This was not the case for the observations used in the Mackay et al. (2011) study, whose time series covered the evolution of the AR two days before and two days after central meridian passage. Second, the cleaned magnetograms describe a smooth, continuous evolution of the photospheric magnetic field, which is numerically easier to simulate. Such a description is a more desirable driver for the magnetofrictional simulation than the noisy uncleaned magnetograms as significant noise and numerical problems can occur in the simulation due to small, rapidly varying unresolved features.

APPENDIX B

CALCULATION OF THE TILT ANGLE

The tilt angle of the AR was calculated by first determining the centers of flux for the positive and negative polarities as a function of time through

$$\mathbf{r}_{\pm} = \left(\int \mathbf{r} B_{\pm} dA \right) \left(\int B_{\pm} dA \right)^{-1},$$

where $\pm$ represents either the positive or negative flux, $\mathbf{r}$ is a position vector and A is the area. The tilt angle (θ) was then calculated by

$$\theta = \arctan \left(\frac{(\mathbf{r}_{-} - \mathbf{r}_{+})_y}{(\mathbf{r}_{-} - \mathbf{r}_{+})_x} \right),$$

where the x and y subscripts denote the x and y components of the vector $\mathbf{r}_{\pm}$.

REFERENCES

Archontis, V. 2008, JGRA, 113, 3
Archontis, V., & Hood, A. W. 2010, A&A, 514, A56
Archontis, V., Moreno-Insertis, F., Galsgaard, K., Hood, A., & O'shea, E. 2004, A&A, 426, 1047
Archontis, V., & Török, T. 2008, A&A, 492, L35
Berger, M. A. 1999, PPCF, 41, B167
Bobra, M. G., van Ballegooijen, A. A., & DeLuca, E. E. 2008, ApJ, 672, 1209
Canfield, R. C., Hudson, H. S., & McKenzie, D. E. 1999, GeoRL, 26, 627
Canfield, R. C., Kazachenko, M. D., Acton, L. W., et al. 2007, ApJL, 671, L81
Cheung, M. C. M., & DeRosa, M. L. 2012, ApJ, 757, 147
Fan, Y. 2001, ApJL, 554, L111
Fan, Y. 2009, ApJ, 697, 1529
Finn, J. M., Guzdar, P. N., & Usikov, D. 1994, ApJ, 427, 475
Glover, A., Ranns, N. D. R., Harra, L. K., & Culhane, J. L. 2000, GeoRL, 27, 2161
Green, L. M., Kliem, B., Török, T., van Driel-Gesztelyi, L., & Attrill, G. D. R. 2007, SoPh, 246, 365
Green, L. M., Kliem, B., & Wallace, A. J. 2011, A&A, 526, A2
Hannah, I. G., Hudson, H. S., Battaglia, M., et al. 2011, SSRv, 159, 263
Hood, A. W., & Priest, E. R. 1981, GApFD, 17, 297
Kliem, B., & Török, T. 2006, PhRvL, 96, 255002
Leake, J. E., Linton, M. G., & Török, T. 2013, ApJ, 778, 99
Liu, Y., Zhao, X. P., Hoeksema, J. T., et al. 2002, SoPh, 206, 333
Longbottom, A. 1998, in ASP Conf. Ser. 150, IAU Colloq. 167: New Perspectives on Solar Prominences, ed. D. F. Webb, B. Schmieder, & D. M. Rust (San Francisco, CA: ASP), 274
Low, B. C., & Lou, Y. Q. 1990, ApJ, 352, 343
Mackay, D. H., & Gaizauskas, V. 2003, SoPh, 216, 121
Mackay, D. H., Green, L. M., & van Ballegooijen, A. A. 2011, APJ, 729, 97
Mackay, D. H., & van Ballegooijen, A. A. 2005, ApJL, 621, L77
Mackay, D. H., & van Ballegooijen, A. A. 2006, ApJ, 641, 577
Magara, T. 2006, ApJ, 653, 1499
Manchester, W., IV, Gombosi, T., DeZeeuw, D., & Fan, Y. 2004, ApJ, 610, 588
Meyer, K. A., Mackay, D. H., van Ballegooijen, A. A., & Parnell, C. E. 2013a, SoPh, 286, 357
Meyer, K. A., Sabol, J., Mackay, D. H., & van Ballegooijen, A. A. 2013b, ApJL, 770, L18
Moreno-Insertis, F. 2004, Ap&SS, 292, 587
Pagano, P., Mackay, D. H., & Poedts, S. 2013, A&A, 554, A77
Pevtsov, A. A., Canfield, R. C., & Metcalf, T. R. 1995, ApJL, 440, L109
Régnier, S., Amari, T., & Kersalé, E. 2002, A&A, 392, 1119
Rust, D. M., & Kumar, A. 1994, SoPh, 155, 69
Rust, D. M., & Kumar, A. 1996, ApJL, 464, L199
Savcheva, A., & van Ballegooijen, A. 2009, ApJ, 703, 1766
Savcheva, A. S., Green, L. M., van Ballegooijen, A. A., & DeLuca, E. E. 2012, ApJ, 759, 105
Seehafer, N. 1978, SoPh, 58, 215
Su, Y., van Ballegooijen, A., Lites, B. W., et al. 2009, ApJ, 691, 105
Titov, V. S., & Démoulin, P. 1999, A&A, 351, 707
Valori, G., Kliem, B., & Keppens, R. 2005, A&A, 433, 335
van Ballegooijen, A. A. 2004, ApJ, 612, 519
van Ballegooijen, A. A., & Martens, P. C. H. 1989, ApJ, 343, 971
van Ballegooijen, A. A., Priest, E. R., & Mackay, D. H. 2000, ApJ, 539, 983
Wheatland, M. S., Sturrock, P. A., & Roumeliotis, G. 2000, ApJ, 540, 1150
Yan, Y., & Sakurai, T. 1997, SoPh, 174, 65
Yan, Y., & Sakurai, T. 2000, SoPh, 195, 89
Yang, W. H., Sturrock, P. A., & Antiochos, S. K. 1986, APJ, 309, 383
Yeates, A. R., Mackay, D. H., & van Ballegooijen, A. A. 2007, SoPh, 245, 87